Actomyosin remodeling regulates biomineral formation, growth and morphology during eukaryote skeletogenesis

Eman Hijaze[1], Tsvia Gildor[1], Ronald Seidel[2], Majed Layous[1], Mark Winter[3], Luca Bertinetti[2], Yael Politi[2] and Smadar Ben-Tabou de-Leon[1,*]

[1]Department of Marine Biology, Leon H. Charney School of Marine Sciences, University of Haifa, Haifa 31905, Israel.

[2]B CUBE Center for Molecular Bioengineering, Technische Universität Dresden, 01309 Dresden, Germany.

[3]Department of Electrical Engineering, Computer Science and Mathematics, Technische Universiteit Delft, Delft 2628CD, Netherlands

*Correspondence: Smadar Ben-Tabou de-Leon (sben-tab@univ.haifa.ac.il)

Abstract (200 words)

Biomineralization is believed to have evolved independently in different phyla, using distinct minerals, organic scaffolds and gene regulatory networks (GRNs). Yet, diverse eukaryotes use the actomyosin network in shaping the biomineral, from unicellular organisms, through echinoderm skeletons to vertebrate bones. Specifically, the actomyosin remodeling protein, Rho-associated coiled-coil kinase (ROCK) regulates vertebrates' chondrocytes, osteoblasts and odontoblasts differentiation and affects gene expression in these biomineralizing cells. Yet, little is known on ROCK role in invertebrates' biomineralization. Here we reveal that ROCK controls the formation, growth and morphology of the calcite spicules in the sea urchin larva. ROCK expression is elevated in the sea urchin skeletogenic cells and its inhibition impairs the organization of F-actin around the spicules, disrupts skeletogenic gene expression and leads to skeletal loss. ROCK inhibition after spicule formation reduces spicule volume and total length, but not thickness and induces ectopic spicule branching. Similar skeletogenic phenotypes are observed when ROCK is inhibited in a skeletogenic cell culture, indicating that these phenotypes are due to ROCK activity specifically in the skeletogenic cells. We propose that the usage of actomyosin network was employed independently, downstream of convergent GRNs across Eukaryotes, to regulate biomineral growth and morphology.

Key words: Biomineralization, Actomyosin remodeling, Sea urchin, ROCK, Skeletogenesis, Gene regulation

Introduction

Biomineralization is the process in which organisms from the five kingdoms of life, use minerals to produce shells, skeletons and teeth that protect and support them [1-8]. Recent studies suggest that biomineralization evolved by the phylum specific co-option of ancestral gene regulatory networks (GRNs) that drove the construction of distinct organic scaffolds [3-5, 8-11] and by the evolution of specialized sets of biomineralization proteins [1, 5, 7, 10, 12-15]. This explanation is in line with the dissimilar GRNs and biomineralization proteins that drive biomineralization in different phyla [3, 14, 16]. Yet, there are common cellular processes required for mineralization in highly diverse phyla [8], suggesting that distinct upstream GRNs might have recruited common molecular mechanisms to drive biomineralization.

The actomyosin network was shown to play a role in biomineralization in various Eukaryote models, from unicellular organisms to vertebrates' bones and teeth [17-24]. The actomyosin network is formed by actin filaments (F-actin), non-muscle myosin II (MyoII), and actomyosin remodeling proteins such as the Rho family GTPases, RhoA, CDC42 and Rac [25-31]. There is a tight association between actin filaments and the biomineralization compartment in diatoms [21] and a highly dynamic actin organization that forms the biomineralization compartment in foraminifera [19]. Perturbations of actin polymerization result with severely deformed shells and inhibition of shell shedding in coccolithophores [17, 18] and diatoms [20]. In vertebrates, Rho GTPases and Rho-associated coiled-coil kinase (ROCK), regulate chondrocytes, osteoblasts and odontoblasts differentiation and affect genes expression in these biomineralizing cells [22-24]. However, the roles of actomyosin remodeling in controlling mineral deposition and shaping biomineral morphology, are still unclear.

Sea urchin larval skeletogenesis provides an attractive model to study the role of the actomyosin network in biomineralization. Sea urchin larval skeletons are made of two frameworks of interconnected calcite rods, termed "spicules" that are generated by the skeletogenic cells [4, 32]. To make the spicules, the skeletogenic cells form a ring with two lateral skeletogenic clusters and fuse through their filopodia forming a pseudopodia cable that links them into a syncytium [33, 34]. The mineral is concentrated in the form of

amorphous calcium carbonate (ACC) inside intracellular vesicles [35]. The vesicles are secreted into the biomineralization compartment generated in the skeletogenic cell clusters forming two triradiate spicules (Fig. 8A, [35, 36]). The tubular biomineralization compartment, also called the spicule cavity, elongates within the pseudopodia cable by localized mineral deposition at the tip of each rod [37].

The GRN that controls sea urchin skeletogenesis is known in great detail and shows notable similarity to the GRN that controls vertebrates' vascularization, suggesting a common evolutionary origin of these two tubulogenesis programs [4, 32, 38, 39]. As the spicules elongate, the expression of key regulatory and biomineralization related genes becomes restricted to the skeletogenic cells proximal to the growing tips, possibly to promote mineral deposition at these sites [40-42]. Localized gene expression is regulated by signaling cues such as the Vascular Endothelial Growth Factor (VEGF) signaling [40, 41]. However, how the skeletogenic GRN drives spicule formation and localized mineral deposition at the tips of the rods is poorly understood.

Previous works suggest that the actomyosin network is essential for skeletal growth and could be regulating mineral deposition in the sea urchin. Calcium bearing vesicles perform an active diffusion motion in the skeletogenic cells with a diffusion length that inversely correlates with the strength and activity of the actomyosin network [43]. Actin filaments are formed around the spicule [43, 44] and F-actin signal is enriched at the tips of the growing skeletal rods in skeletogenic cell culture [45]. Genetic and pharmacological perturbations of the GTPase, CDC42, prevent the formation of filopodia in the skeletogenic cells and inhibit spicule formation and elongation [46]. Pharmacological perturbations of ROCK prevent spicule formation [47] and genetic perturbations of Rhogap24l/2 result with ectopic spicule splitting [4]. Despite these phenotypic characterizations, little is known on the regulation and role of the actomyosin network and remodeling proteins in localized mineral deposition.

Here we study the spatiotemporal pattern of ROCK expression, investigate the role of ROCK in mineral uptake and deposition, study the role of ROCK and the actomyosin network in skeletal growth and morphology and investigate the effect of ROCK inhibition on skeletogenic gene expression, in the sea urchin *Paracentraorus lividus (P. lividus)*. Our

findings reveal the critical role of ROCK and the actomyosin network in multiple aspects of sea urchin biomineralization, suggesting a common use of the actomyosin network in Eukaryote biomineralization, downstream of distinct GRNs.

Results

ROCK is enriched in the skeletogenic cells, partially depending on VEGF signaling

We sought to study the expression and cellular localization of the ROCK protein and its regulation by VEGF signaling, a prominent regulator of sea urchin skeletogenesis [4, 38, 39]. The sequence of ROCK and especially, its functional domains are highly conserved between human and sea urchin (Fig. S1). We therefore used a commercial antibody that recognizes human ROCK protein to test ROCK expression in *P. lividus* embryos (Fig. S2). We first extracted proteins from whole embryos and used western blot to detect ROCK expression in control and under VEGFR inhibition at the time of spicule formation and during skeletal elongation (~22 hours post fertilization [hpf], 27hpf and 33hpf, Fig. S2). The antibody detected a ~150kDa protein (Fig. S2A) that is the predicted size for *P. lividus* ROCK protein (153kDa). VEGFR inhibition marginally increased the overall level of ROCK at 22hpf, but did not affect it at 27hpf and 33hpf (Fig. S2B). Yet, this measurement was done on proteins extracted from whole embryos, and we wanted to study the spatial expression of ROCK and specifically, its regulation in the skeletogenic cells.

We studied the spatial distribution of ROCK protein within the sea urchin embryo, using ROCK antibody and the skeletal marker, 6a9, that marks the skeletogenic syncytium membrane ([48], Fig. 1). We quantified ROCK signal in the skeletogenic cells compared to the neighboring ectodermal cells in control embryos and under VEGFR inhibition, at the three time points mentioned above. At 22hpf, ROCK expression in the skeletogenic cells is mildly enriched compared to the neighboring ectodermal cells and this enrichment is not observed under VEGFR inhibition (Fig. 1A-F). At 27hpf, ROCK enrichment in the skeletogenic cells increases, but similar enrichment is observed under VEGFR inhibition (Fig. 1G-L). At 33hpf, ROCK enrichment in the skeletogenic cells is most apparent (Fig. 1M-O). A much weaker skeletogenic enrichment is observed under VEGFR inhibition, suggesting that continuous VEGF signaling is required for ROCK upregulation in the skeletogenic cells (Fig. 1P-S). At both 27hpf and 33hpf in control embryos, ROCK seems

localized near the skeletogenic cell membranes, which further supports its activation in these cells, since ROCK activation leads to its localization to the cell membranes in other systems [49]. Overall, this data demonstrate that ROCK expression is elevated in the skeletogenic cells and this enrichment strengthens with skeletal elongation and partially depends on VEGF signaling.

ROCK activity in the skeletogenic cells controls spicule initiation, growth and morphology

Next, we studied the role of ROCK in sea urchin skeletogenesis using genetic perturbations. We downregulated the expression of ROCK by the injection of two different morpholino anti-sense oligonucleotides (MASOs) that block the translation of the gene at two different regions. ROCK MASO-1 matches the start of translation region, ROCK MASO-2 matches the 5' region upstream the start of translation, and random MASO was used as a control (see methods for details). The two ROCK MASOs induced substantial skeletogenic phenotypes compared to the control MASO (Fig. 2A-E). Embryos injected with either ROCK MASO-1 or MASO-2 show strongly reduced skeletons (Fig. 2C, D) and embryos injected with ROCK MASO-2 show an additional phenotype of severely branched skeleton (Fig. 2B). The additional branching phenotype and the larger percentage of affected embryos in ROCK MASO-2 are probably due to its higher efficiency resulting from its more 5' location relative to translation start codon (Fig. 2E). Thus, the genetic perturbations of ROCK expression indicate that sea urchin ROCK is important for skeletal elongation and normal branching.

To elucidate the dosage dependence of ROCK activity and identify its effect on different stages of skeletogenesis, we tested the skeletogenic phenotypes of different concentrations of ROCK inhibitor, Y27632, applied before or after spicule initiation (Fig. 2F). Y27632 binds to the ATP site of ROCK's kinase domain and prevents its activity [50]. The amino-acids to which Y27632 binds, are conserved in the sea urchin ROCK protein, supporting its specific inhibition of this protein (Fig. S1C).

The concentration and timing of ROCK inhibition leads to diverse skeletogenic phenotypes suggesting multiple roles of ROCK activity in sea urchin skeletogenesis (Fig. 2G-P, S3). Continuous ROCK inhibition, beginning at egg fertilization, using 80µM Y27632, did not

affect skeletogenic cell migration but eliminated skeletal formation at 27hpf (Fig. 2G, H). At two days post fertilization (dpf) the majority of the embryos completely lack skeleton and the rest show only spicule initiations, yet their overall embryonic development seems normal (Fig. 2J, P, in agreement with [47]). Similar results are observed when adding the inhibitor in this concentration at 20hpf (Fig. 2K, P). Yet, the addition of 80µM of the inhibitor at 25hpf, after spicule initiation, results in a majority of embryos with severe ectopic spicule branching, which resembles the branching phenotype observed in ROCK MASO-2 (Fig. 2L, P). Reducing the concentration of the added inhibitor leads to milder branching and elongation phenotypes (Fig. 2M, N, P, S2). However, even at the lowest inhibitor concentration, we detect a reduction of skeletal growth rate and ectopic branching a few hours after the addition of ROCK inhibitor (Fig. S4, 30µM). Washing the inhibitor after 25hpf results in partial recovery of skeletogenesis, with normal or mildly delayed skeletons (Fig. 2O, P, S3). Overall, our genetic and pharmacological perturbations indicate that ROCK activity is necessary for spicule formation, skeletal elongation and normal branching pattern.

The pharmacological and genetic perturbations we carried, affect ROCK expression in all the cells of the embryo. To test if ROCK activity specifically in the skeletogenic cells underlies ROCK skeletogenic phenotypes, we inhibited ROCK in a culture of isolated skeletogenic cells (Fig. 3). *P. lividus* skeletogenic cells were isolated and cultured as described in [45]. The addition of ROCK inhibitor to the skeletogenic cell culture at 16hpf completely abolished spicule formation (Fig. 3B). The addition of the inhibitor after spicule initiation, which is 48hpf in the skeletogenic cell culture, resulted with significantly shorter spicules (Fig. 3C, E), that show more branching than control spicules (Fig. 3D). The reduction of the spicule length depends on the concentration of the ROCK inhibitor (Fig. 3E). Overall, ROCK skeletogenic phenotypes in the isolated skeletogenic cell culture are similar to its phenotypes in whole embryos, verifying that it's specific activity in the skeletogenic cells is essential for spicule formation, normal elongation and prevention of branching.

ROCK inhibition reduces spicule volume, surface area and total length, but not thickness (SR-µCT)

To quantify the effect of ROCK inhibition on mineral deposition and skeletal shape we used synchrotron radiation micro-computed tomography (SR-µCT) that enables three-dimensional visualization and quantification of spicule morphology at 2 and 3dpf (Figs. 4, S5, see methods for details). The aberrant morphology of ROCK inhibited spicules is visible at both developmental time points (Fig. 4A). The ectopic branching occurs both at the tips, where we observe tip-splitting (arrowheads, Fig. 4A), as well as in the back, where we observe small spicule extensions, or spicule 'dripping' (arrow at 48hpf, Fig. 4A). This implies that the localization of mineral deposition is perturbed both at the tip and in the back of the spicules under ROCK inhibition.

When compared to control spicules, ROCK inhibition leads to a ~2.5-fold reduction of the spicule volume and surface area in both 2 and 3dpf (Fig. 4B-D): The mean volume of control spicules at 2dpf is 6,850 μm^3±2,000 μm^3 compared to 2,925 μm^3±974 μm^3 under ROCK inhibition. The mean volume of the spicules at 3dpf is 14,673 μm^3±2,747 μm^3, compared to 5800 μm^3±2409 μm^3 in ROCK inhibition (see Table S2 for details and S3 for statistical analyses). Similar trends were measured for surface area (2dpf control, 5823μm^2±1122μm^2, ROCK inhibition, 2335μm^2±607µm2; and 3dpf control, 9897μm^2±1200 μm^2, ROCK-inhibition, 4003μm^2±1250μm^2. See tables S2 and S3). These SR-µCT measurements show that the rate of mineral deposition is significantly reduced under ROCK inhibition.

To understand the specific effect of ROCK inhibition on spicule elongation vs. thickening, we compared the total length and the mean thickness of the spicules between control and ROCK inhibition (Fig. 4E-G). The total length of control spicules was on average about 2.5-times longer than the length under ROCK inhibition in both 2dpf and 3dpf (2dpf control: 497µm±62µm, ROCK inhibition: 188µm±50 µm; and 3dpf control: 697µm±71µm, ROCK inhibition: 276µm±81µm. Fig. 4E, F, tables S2 and S3). In contrast to its effect on the spicule length, ROCK inhibition caused a minor increase of the spicule thickness at 2dpf, that is statistically significant (2dpf control: 3.7µm±1.4µm, ROCK inhibition: 3.9µm±1.6 µm). At 3dpf the thickness was not affected by the inhibition (3dpf control: 4.4µm±2 µm, ROCK inhibition: 4.4µm±1.7 µm, Fig. 3E, G, Table S2, S3). These SR-µCT measurements indicate that ROCK activity plays a crucial role in controlling the

localization and rate of mineral deposition at the tips of the rods and preventing ectopic spicule branching at the tips and in the back of the spicules.

ROCK activity does not control mineral uptake but is required for "tip-dominance"

To test the effect of ROCK inhibition on mineral intake, we used the fluorescent chromophore, calcein that binds to divalent ions including Ca^{+2} and is widely used to track the calcium pathway in biomineralization [4, 36, 42, 43]. We measured the number of calcium vesicles per area as well as the number of pixels of calcein signal per area in the skeletogenic cells, in control and under ROCK inhibition at 1dpf and 2dpf (Fig. S6A-E). Continuous ROCK inhibition does not change the number of calcium bearing vesicles at 1dpf, but the number of calcein stained pixels significantly increases in this condition, possibly indicting that the vesicle volume is larger (Fig. S6F, G). At 2dpf, the number of calcein stained pixels is similar in control and in continuous ROCK inhibition, suggesting that the overall calcium content does not change in this condition (Fig. S6H, I). The number of calcein stained vesicles is decreased under ROCK inhibition, possibly indicating that there are fewer vesicles with larger volume. Addition of ROCK inhibitor at 25hpf affects neither the number of calcein stained vesicles nor the number of calcein stained pixels in the skeletogenic cells. Together, these measurements show that ROCK is not required for the uptake of calcium into the cells. Therefore, the skeletal phenotypes occurring under ROCK inhibition are not related to a decrease in calcium uptake or shortage in intracellular calcium.

To monitor the effect of ROCK inhibition on mineral deposition rate and distribution, we applied two pulses of different calcein dyes: blue calcein was added at 29hpf and washed after one hour, followed by green calcein added at 44hpf and washed after one hour. Hence, blue calcein marks the initial triradiate region and green calcein marks the edges of the spicules that were recently deposited (blue and green arrows in Fig. 4H, I). The dye FM4-64 was used to mark the cell membranes. Under ROCK inhibition, the green labeled region is much closer to the blue labeled region compared to control, due to the reduction in skeletal elongation rate, in agreement with our SR-µCT measurements. However, while in control embryos each body rod has a single tip stained in green calcein, under ROCK inhibition one of the body rods has two tips and both are stained in green. This indicates

that mineral is being deposited in both edges, and the mechanism that prevents the growth of multiple tips in each rod, enabling "tip-dominance", is disrupted under ROCK inhibition.

F-actin is essential for normal spicule elongation and inhibition of ectopic branching

In other systems, major roles of ROCK are to control F-actin stabilization and MyoII activation [25, 51-54], hence we wanted to directly test the role of these actomyosin components in sea urchin skeletogenesis. To directly inhibit F-actin polymerization we used Latrunculin-A (Lat-A), that prevents the polymerization of actin monomers [55] and was shown to be effective in sea urchin embryos [56]. To directly inhibit actomyosin contractility we used Blebbistatin (Blebb), that interferes with MyoII ATPase activity, prevents actin-myosin interactions [57] and was shown to be effective in sea urchin embryos [58]. To prevent interference with the early cell divisions where the actomyosin network plays a critical role [59-61], we added the inhibitors, individually or together, before or after spicule formation (20hpf and 25hpf, Fig. S7A, see methods for details). We tested the resulting phenotypes at 2dpf (Fig. S7B-I).

Our results indicate that F-actin polymerization is essential for normal skeletal growth and inhibition of ectopic branching, while actomyosin contractility plays a minor role in these processes (Fig. S7). The majority of the embryos where MyoII activation was inhibited show minor ectopic branching mostly at the tips of the rods, and some embryos show a delay in skeletal growth (Fig. S7C, D, I). The majority of the embryos where F-actin formation was inhibited show significant reduction of skeletal growth and severe ectopic skeletal branching (similar phenotypes to Fig. S7E, statistics in Fig. S7I). Some embryos show completely arrested skeletal growth (Fig. S7G, I) and in some embryos, additional spicules form (Fig. S7H, I). The co-inhibition of F-actin polymerization and MyoII activity results in skeletogenic phenotypes that resemble those of the inhibition of F-actin alone (Fig. S7I). These results indicate that F-actin polymerization is essential for normal skeletal growth and inhibition of ectopic branching throughout skeletogenesis, while MyoII has a minor role in the late stage of these processes.

Strong reduction of skeletal growth and enhanced ectopic branching are common phenotypes to ROCK inhibition and to F-actin inhibition (Figs. 2K-N, P, compared to S7E-G, I). Yet, ROCK inhibition before spicule formation completely blocks skeletogenesis in

the majority of the treated embryos (Fig. 2J, P), which was never observed in actomyosin perturbations (Fig. S7). These observations suggest that ROCK's effect on skeletal growth and branching could be through its regulation of F-actin stabilization, but its role in spicule initiation is possibly mediated through its other targets.

ROCK activity is required for F-actin organization around the forming spicule

Next, we tested whether ROCK regulates the actomyosin structure and activity during sea urchin skeletogenesis. To accomplish this we used phalloidin, a fluorophore that binds F-actin specifically, an antibody that detects phosphorylated MyoII (MyoIIP, [43]) and the skeletogenic marker, 6a9 (Fig. 5). In control embryos, F-actin is detected around the tri-radiate calcite spicules at 27hpf (green arrow in Fig. 5B, in agreement with [43, 44]). The pseudopodia cable that connects the skeletogenic cells shows lower F-actin signal compared to the signal around the spicule (blue line in Fig. 5B, C, E blue arrows in Fig. 5I, J, L). This could indicate that F-actin accumulates around the membrane of the spicule cavity that face the mineral, which does not exist in the pseudopodia cable. MyoIIP signal is not enriched in the skeletogenic cells nor in the spicule (Fig. 5D, K). Under continuous ROCK inhibition, the pseudopodia that connects the skeletogenic cells still forms (Fig. 5T) and F-actin accumulation is still observed in the lateral skeletogenic cell clusters; but unlike control embryos, F-actin is not organized and the spicule cavity is not formed (Fig. 5N). MyoIIP signal seems unchanged by ROCK inhibition (Fig. 5P, U), in agreement with the weak and late phenotype of MyoII inhibition (Fig. S7). These findings suggest that ROCK activity is essential for F-actin organization around the spicules, but not for the formation of the pseudopodia cable.

F-actin is enriched at the tips of the spicules independently of ROCK activity

To assess the role of ROCK in actomyosin organization during skeletal elongation we compared F-actin and myoIIP signals between control embryos and embryos where ROCK inhibitor was added at 25hpf (Fig. 6). At the prism stage, F-actin is enriched at the tips of the spicules in both control and ROCK inhibited embryos (white arrowheads in Figs. 6B-E, F-J). We quantified the F-actin signal at the tips compared to the back in both treatments (Fig. 6K, L, see methods for details). The phalloidin signal is on average 3-fold stronger at the tips of the spicules compared to the back, in both control and ROCK inhibition,

indicating that F-actin enrichment at the tips is significant and independent of ROCK activity. In both control and ROCK inhibited embryos, the F-actin signal was markedly higher in the regions of the pseudopodia cable where the spicule cavity had formed, compared to the regions where the spicule cavity had not yet formed (blue arrows in Fig. 6B-E, G-J). This again, suggests that F-actin accumulates near the inner membrane of the spicule cavity that surrounds the mineral. We did not detect an enhanced signal of MyoIIP around the spicules or in the skeletogenic cells, in either condition (Fig. 6D, I). Together these data demonstrate that F-actin coats the spicule cavity, probably near the membrane facing the mineral, and is enriched at the tip of the rods, independently of ROCK activity.

At the pluteus stage, F-actin is enriched at the tips of the spicules in both control and ROCK inhibited embryos (white arrowheads in Fig. 6N-Q, S). Some non-skeletogenic cells that are enriched with MyoIIP signal are detected at this time (red arrowheads in O-R). Thus, F-actin enrichment at the tips of the rods correlates with calcium deposition there, but this enrichment does not depend on ROCK activity.

ROCK activity is essential for normal skeletogenic gene expression

The role of ROCK in regulating gene expression during vertebrates' chondrocytes, osteoblasts and odontoblasts differentiation [22-24] intrigued us to study the role of ROCK in regulating skeletogenic gene expression in the sea urchin embryo. ROCK continuous inhibition significantly downregulates the expression of multiple skeletogenic genes, including the cytoskeleton remodeling gene, *rhogap24l/2*, the biomineralization genes, *caral7*, *scl26a5* and *SM30* at 27hpf and 2dpf (Fig. 7A, [4]). ROCK inhibition did not affect the expression level of VEGFR and ROCK itself at these times (Fig. 7A). Washing the inhibitor after 25hpf or adding the inhibitor at 25hpf had a weaker effect, but still led to downregulation of *caral7*, *SM30*, *angio1* and *notch1* (Fig. 7B). Thus, ROCK activity is required for the activation of multiple skeletogenic genes during sea urchin skeletogenesis.

Both continuous and late ROCK inhibition, strongly affects the spatial expression of key regulatory and biomineralization genes that are normally expressed differentially within the skeletogenic lineage at the pluteus stage (Fig. 7D-L). These include, the skeletogenic transcription factors, Ets1, Alx1 and Erg1 that are essential for skeletogenic cell specification and biomineralization [32, 62], the transcription factors Hex and MyoD1,

VEGF receptor (VEGFR) and the biomineralization genes *SM50* and *SM30*. In normal plutei these genes are differentially expressed within skeletogenic lineage, but in both continuous and late ROCK inhibition the expression of these genes becomes localized to the two lateral skeletogenic cell clusters and their vicinity (Fig. 7D-L). The lateral skeletogenic cells clusters are the cells where these genes are expressed in the gastrula stage (24-27hpf) and where spicule formation begins in normal embryos [4, 41]. The expression of VEGFR and SM50 under ROCK inhibition is more expanded than the other tested genes and is also observed at the tips of the anterolateral rods (Fig. 7I, K). The VEGF ligand that is normally expressed in the ectodermal cells near the four tips of the post-oral and anterolateral rods [41], is expressed at four ectodermal domains near the lateral skeletogenic cell clusters and near the end of the anterolateral chain, under ROCK inhibition (Fig. 7J).

Overall, under ROCK inhibition, the expression of key regulatory and biomineralization genes is downregulated (Fig. 7A) and remains localized to the area near the lateral skeletogenic cells clusters (Fig. 7D-I, K, L). This localization is despite the proper formation of the dorsal, anterolateral and mid-ventral chains (Fig. 7C). This implies that ROCK activity provides regulatory cues to the skeletogenic GRN required for the dynamic progression of gene expression within the skeletogenic lineage.

Discussion

Biomineralization is a complex molecular process, encoded in the species genome and executed by the GRNs and the cellular machinery. Here we used the sea urchin larval skeletogenesis to investigate the role of ROCK and the actomyosin network in biomineral formation and in regulating gene expression, as we summarize in Fig. 8. ROCK expression is enriched in the skeletogenic cells, partially depending on VEGF signaling (Figs. 1). ROCK activity in the skeletogenic cells is necessary for spicule formation, skeletal elongation and prevention of ectopic skeletal branching (Figs. 2-4, S4). Direct inhibition of F-actin polymerization results in similar but not identical skeletogenic phenotypes (Fig. S7) and F-actin is organized around the spicule cavity and enriched at the spicule tips (Figs. 5, 6). ROCK activity feeds back into the skeletogenic GRN and affects regulatory and

biomineralization gene expression (Fig. 7). Below we discuss our findings and their implications for the biological control and evolution of biomineralization.

The first step in generating the sea urchin spicules is the construction of the spicule cavity, a membrane filled with calcium carbonate and coated with F-actin (Fig. 8A). ROCK activity is necessary for the formation of the spicule cavity and for the organization of F-actin around it (Figs. 2, 5, 8B). A direct perturbation of F-actin polymerization strongly disrupts spicule growth and shape (Fig. S7). F-actin is enriched in the regions of the pseudopodia cable that are filled with mineral, supporting its localization near the inner membrane of the spicule cavity (Figs. 5, 6, Fig. 8A). F-actin accumulation near the inner membranes of the spicule cavity could be providing cues and structural support for the exocytosis of mineral-bearing vesicles into the cavity, as we explain below (Fig. 2H, [29-31, 63]). Overall, our studies indicate that ROCK activity in the skeletogenic cells is essential for the formation of the spicule cavity and for the initial F-actin organization around it, which could be essential for mineral deposition into it (Fig. 8C).

After the spicule cavity has formed, the spicules elongate inside the pseudopodia chord by mineral deposition at the tips of the spicule rods, which depends on ROCK activity and on F-actin polymerization (Figs. 2-4, S7, 8E, F). F-actin is detected along the spicules and is significantly enriched at the tips of the elongating spicules (Fig. 8D, [29]). F-actin enrichment at the tips is independent on ROCK activity (Fig. 6A-M, 8E, F), yet under ROCK inhibition and under the inhibition of F-actin polymerization, ectopic branching is observed at the tips and in the back (tip splitting and spicule dripping, Figs. 2P, 3D, 4A, S7I). The participation of F-actin and ROCK in polarized tip-growth and vesicle exocytosis has been observed in both animals and plants [29, 64]. F-actin is used for short range myosin trafficking of vesicles toward the secretion site [29, 63]. Once the secretory vesicle fuses with the membrane, it is coated with F-actin that stabilizes the vesicle and enables MyoII binding and ROCK-regulated contraction, necessary for content secretion [30, 31]. In plant cells, F-actin accumulate at the growing tip of the cell and assists vesicle exocytosis necessary for polarized tip-growth [64]. Our observations suggest that ROCK and F-actin could be regulating the localized exocytosis of mineral-bearing vesicles during sea urchin skeletogenesis. The delay in spicule growth and the ectopic branching could be due to

impaired and misplaced vesicle trafficking and deposition under ROCK and F-actin inhibition, but the exact protein regulatory network is still to be determined.

ROCK activity is necessary for correct spatiotemporal expression of regulatory and biomineralization genes (Fig. 7, 8D-F). ROCK inhibition downregulates the expression level of skeletogenic genes (Fig. 7A) and prevents the spatial progression of key skeletogenic genes toward the edges of the skeletal rods (Fig. 8E). In other systems, ROCK activity was shown to regulate gene expression through various intracellular pathways including YAP, SRF and extracellular signal-regulated kinase (Erk) [65-67]. Furthermore, ROCK has an important role in mechano-sensing of matrix rigidity and transducing it into changes in gene expression [68]. Relatedly, stiff matrix activates ROCK in pre-osteoblastic cells, which activates Erk that leads to osteogenic differentiation and upregulation of osteogenic gene expression [67]. Sea urchin ROCK could be sensing the spicule stiffness and transducing it into gene expression, providing a necessary feedback between spicule elongation and the skeletogenic GRN. Further studies are required to identify the specific molecular mechanisms activated by ROCK to affect gene expression in the skeletogenic cells.

Overall, our findings and the role of actomyosin remodeling in biomineralization, from calcifying and silicifying single cells to vertebrates' bones and teeth [17-24, 67], suggest that this molecular machinery is a part of the common molecular tool-kit of biomineralization. Most likely, the actomyosin network was employed independently, downstream of convergent GRNs across Eukaryotes, to control mineral deposition and shape biomineral morphology.

Methods

Animal and embryos

Adult *Paracentrotous lividus* were obtained from the Institute of Oceanographic and Limnological Research (IOLR) in Eilat, Israel. The animals were kept in aquaria in a dedicated room, in artificial seawater (ASW) with the salinity of 39 ppt. Eggs and sperm were obtained by injection of 0.5M KCl solution into the adult sea urchin species. Embryos were cultured at 18°C in 0.2µ filtered ASW.

Imaging

Embryonic phenotypes and WMISH were imaged by Zeiss Axioimager 2. Fluorescent markers were imaged using Nikon A1-R Confocal microscope. All images were aligned in Adobe photoshop and Illustrator.

Axitinib (AG013736) treatment

5mM stock solution of Axitinib (AG013736, Selleckchem, Houston, TX, USA), was prepared by reconstituting the chemical in dimethylsulfoxyde (DMSO). The embryos were treated with Axitinib at a final concentration of 150nM. Control embryos were cultured in similar concentrations of DMSO at no more than 0.1% (v/v).

Western Blot

Embryo cultures treated with 150 nM Axitinib, or DMSO as control, were collected at 22hpf, 27hpf and 33hpf by centrifugation of 10,000g for 2 minutes. We lysed the pellet in 150µL lysis buffer (20 mM Tris-HCl, 150 mM NaCl, 1% Triton X-100, pH 8) with protease inhibitors (protease inhibitor cocktail w/o metal chelator; Sigma, P8340; 1:100) and phosphatase inhibitors (50 mM NaF, 1 mM Na3VO4, 1 mM Na4P2O7, 1mM, βGP) as described in [69]. 40µg protein were loaded on 8% SDS-acrylamide gel, transferred to PVDF membranes for Western blot analysis. Anti-ROCK antibody (ab45171, Abcam) was used in a 1:300 dilution followed by anti-rabbit HRP secondary antibody diluted to 1:2500 (Jackson ImmunoResearch 111-035-003). For the loading control, the membrane was incubated with anti-β-tubulin antibody (1:5000; Sigma) followed by anti-mouse antibody 1:5000 (Jackson ImmunoResearch 115-035-003). Quantification of ROCK signal was done using Image studio lite vr. 5.2. ROCK signal was divided by Tubulin signal and then the ratio between ROCK/Tubulin in control vs. VEGFR inhibition was calculated. The graph in Fig. S2 was generated based on three biological replicates (different sets of parents) at 27hpf and 33hpdf and four biological replicates at 22hpf.

Immunostaining procedure

Phalloidin labeling, MyoIIP (p20-MyosinII), ROCK (anti ROCK2+ROCK1 antibody [EP786Y], AB-ab45171, Abcam), and 6a9 immunostaining were done similarly to [43].

Quantification of Anti-ROCK and Phalloidin signal

A graphical program was written to allow manual quantification of the fluorescent signal from the spicule regions by identifying "stained" pixels per selected area. For ROCK immunostaining, embryos at 22hpf, 27hpf and 33hpf in control and under VEGFR inhibition were used, and regions in the skeletogenic cells or in the ectoderm were selected. A global threshold was chosen to identify the "stained" pixels. The ratio of stained anti-ROCK to region total area was compared between ectodermal and skeletogenic cells, and between control and VEGFR inhibited embryos. For phalloidin analyses, embryos at 33hpf of control and ROCK inhibitor addition at 25hpf were used and for each image, two regions were selected: an area at the tip of the spicule and an area at the back of the spicule, about ~10 microns apart. The ratio of stained phalloidin to region total area was compared between tip and back, in control and ROCK inhibited embryos. Paired t-test was used to compare the differences in phalloidin signal between the tip and back of the spicules across all groups. t-test was used to compare tip/back ratio of Phalloidin signal between control and ROCK inhibited embryos.

ROCK MASOs injections

Microinjections were conducted similarly to [41]. The eggs were injected with an injection solution containing 0.12M KCl, 0.5µg/µl Rhodamine Dextran and 900µM of MASOs. Downregulation of *ROCK* was done by injecting two specific MASOs targeting the translation sites of the pre-mRNA. MOSOs were designed and synthesised by Gene Tools, Philomath, OR, according to ROCK sequence. The sequence of ROCK MASO-1 (5'-AGACATATTTGGAGCCGACATCCTG-3') matches the start of translation region (ATG, marked in green), and ROCK MASO-2 (5'-TCTCTTGCGTTATATTCCACTAAGT-3') that matches the 5' region upstream of the start of translation. Control embryos were injected in the same concentration with Random MASO. Injected embryos were cultured at 18°C, imaged and scored at 2dpf.

ROCK inhibitor (Y27632) treatment

Y27632 is a specific inhibitor to the ATP site of ROCK's kinase domain and competitively inhibits the phosphorylation of its targets (28). Y27632 stock (10005583 CAS Regisrty No.

129830-38-2, Cayman chemical), was prepared by reconstituting the chemical in dimethylsulfoxyde (DMSO). The embryos were treated with Y27632 at a final concentration between 30-80µM, as mentioned in the results. When we wanted to investigate the branching pattern in the inhibitor-addition experiments we used 30-40µM, which leads to large spicules with prominent ectopic branching (Fig. 2P). In the continuous experiments we mostly used 80µM, which gives a robust phenotype of either spicule loss or spicule initiations (Fig. 2P). Throughout the paper, control embryos were cultured in DMSO at the same volume as Y27632 solution and no more than 0.1% (v/v).

ROCK inhibition in isolated skeletogenic cell culture

Skeletogenic cell culture was performed as described in [45] with minor changes. Isolated skeletogenic cells were cultured in CultureSlides (4 chambers polystyrene vessel tissue culture treated glass slide REF 354104) with ASW (Red Sea Fish LTD) containing Gentamicin and Penicillin-Streptomycin (GPS) at 18°C. Media containing 4% (v/v) horse serum (Sigma-Aldrich H1270) in ASW+GPS was added to the culture. ROCK inhibitor, Y27632, was added to the cell culture at 16hpf (before spicule initiation) or 48hpf (after spicule initiation), and images were taken at 72hpf. Each treatment was conducted in three biological repeats except from the >48hpf addition of 120µM which was done in two biological repeats.

Quantification of skeletal length and statistical analysis

Skeletal length measurement was done as described in [41]. The measurements were repeated for three biological repeats for control, ROCK inhibition with 30µM and 80µM and 2 biological repeats for 120µM. A total of 275 skeletons were measured for control, 105 skeletons for 30µM, 122 skeletons for 80µM and 80 for 120µM. The data were analyzed in Excel and the statistical analysis was performed using Kruskal-Wallis non-parametric test in Excel as described in [70] and SPSS statistics 27.

Spicule preparation for micro-computed tomography (SR-µCT) measurement

Control embryos and embryos where 40µM Y27632 was added at 25hpf, were collected by centrifugation of 50mL Falcon tubes at 2000rpm, at 48h and 72hpf. Every tube was washed in 10 mL cold distilled water (DW), transferred into epi-tube and washed three

times in 1mL cold DW (incubation at 4˚C between every wash, centrifuge at 2000rpm in room temperature for 2min). Then the skeletons were washed three times in 3% NaOCl followed by three washes in DW, one wash in 70% EtOH and one wash in Acetone. Skeletal spicules were dried at room temperature and stored at -20 ˚C.

Synchrotron and lab-based SR-µCT

Dry and loose skeletal spicules prepared as described above, were used for the SR-µCT analysis. We analyzed 14 sets of spicules from three (control) and four (ROCK inhibited) pairs of parents, divided into four groups: 2dpf, control, n=44; 2dpf ROCK inhibited, n=93; 3dpf control, n=51; 3dpf ROCK inhibited, n=93, see Table S1). Spicules were glued to sharpened toothpick tips, either in bulk ('rinsing' spicules over the liquid glue) or individually when picked by hand by means of a brush bristle. Each toothpick loaded with spicules, was mounted on a 3ml vial twist-off lid and for transportation securely stored in the vial (Fig. S5A, B). Typically, hundreds to a dozen spicules were attached to tooth picks in bulk and individual preparations, respectively. For each set 2-3 µCT-samples were prepared, which allowed the acquisition of statistically relevant sample sizes (40+ spicules/group, Table S1). Tomographic data sets were acquired using the following scanning parameters; for the lab based µCT (RX Solutions, Chavanod, France) 90kV, 143-160µA, 1440 images, average frames 10, frame rates 0.4-1, voxel sizes: 0.45-59µm; and for the synchrotron radiation µCT (Anatomix, Synchrotron SOLEIL, Gif-sur-Yvette, France) 2048 images, angle between projections 0.09°, voxel size: 0.65µm. Tomographic data reconstruction was performed with commercial (RX Solutions, Chavanod, France) and PyHST2 software (A. Mirone et al., Nucl. Instrum. Meth. B 324 (2014) 41-48, doi:10.1016/j.nimb.2013.09.030) at the MPICI and at Anatomix, SOLEIL, respectively.

Three-dimensional (3D) data analysis

Data visualization, pre-processing including cropping and image type conversion to 16bit (of the Sr- µCT data), and user-augmented segmentation of intact spicules were performed in Amira using off-the-shelf modules (Fig. S5C-E, [71]). The grey level segmentation of the spicules was mostly done with the same threshold value on the greyscale across all data sets. Volume and area measurements were performed on the segmented spicules, *i.e.* the

label-fields using Amira's material.statistics module (Volume3D and Area3D). Average spicule thickness and total length measurements were performed with python code, utilizing available python libraries (*e.g.*, skimage, skan, scipy). The code was applied to 3D-tif files created from Amira's label-fields, which contained the segmented spicules. For length measurements, the spicules were skeletonized and the chord lengths of the branches forming a spicule-skeleton were summed up to obtain the total spicule length. For thickness measurements, we performed Euclidean distance transforms for each spicule using scipy's ndimage.morphology.distance_transform_edt package, and calculated the average spicule thickness based on the distance measurements obtained at each voxel from spicule-skeleton to the nearest spicule surface. Quality control of our measurements was performed with open source software, Fiji and available plugins (e.g. BoneJ, FiberJ, DiameterJ).

Calcein staining

A 2mg/ml stock solution of blue calcein (M1255, Sigma) and a 2mg/ml stock solution of green calcein (C0875, Sigma) were prepared by dissolving the chemicals in distilled water. Working solution of 250µg/ml and 150µg/ml, respectively, was prepared by diluting the stock solution in artificial sea water. Blue calcein was added to the embryo culture at 29hpf for one hour and then washed. At 44hpf the green calcein was added for one hour and washed. For FM4-64 staining A 100µg/ml stock solution of FM4-64 (T13320, Life technologies, OR, USA) was prepared by dissolving the chemical in distilled water. Working solution of 2.5 µg/ml was prepared by diluting the stock solution in artificial sea water. Embryos were immersed in working solution about 10 minutes before visualization.

Latrunculin-A and Blebbistatin treatments

1mM of Lat-A stock (L12370, Thermo Fisher Scientific) was prepared by reconstituting the chemical in DMSO. The embryos were treated with Lat-A at final concentration of 2 µM. 1mM of Blebbistatin stock (13013-5, Enco) was prepared by reconstituting the chemical in DMSO. The embryos were treated with Blebbistatin at final concentration of 2 µM. For the double inhibition experiments, embryos were treated with Blebb at final concentration of 1.5 µM, and with Lat-A at final concentration of 2 µM.

WMISH procedure

WMISH was performed as described in [39, 41]. List of the primers used to make the WMISH probes is available in [41].

cDNA preparation for QPCR experiments

For ROCK inhibition experiments total RNA was extracted from >1000 sea urchin embryos in each condition using RNeasy Mini Kit (50) from QIAGEN (#74104) according to the kits' protocol. DNase treatment on column was done using RNase-Free DNase Set-Qiagen (50) (#79254). RNA was reverse-transcribed using the High Capacity cDNA RT kit, AB-4368814 (Applied Biosystems) following the manufacturer's instructions.

Quantitative polymerase chain reaction (QPCR)

QPCR was carried out as described in [41]. Complete list of primer sequences used for the experiments in provided there.

Acknowledgments

We are grateful to SOLEIL for provision of synchrotron radiation facilities and we would like to thank Dr. Mario Scheel, Dr. Timm Weitkamp and Dr. Jonathan Perrin for assistance in using beamline ANATOMIX for nano and µCT. We thank the Bioimaging Unit, Faculty of Natural Sciences, University of Haifa for assistance with the use of confocal. We thank Charles Ettensohn for the generous gift of the 6a9 antibody produced in his lab. We thank David Ben-Ezra and Michael Kantorovitz for their help with sea urchin handling. We thank Haguy Wolfenson for illuminating discussions of the results and conceptual framework. We thank Nir Sapir and Tovah Nehrer for their advice and help with the statistical analysis of spicule length. We thank Alvaro Israel and Omri Nahor for their help with sea urchin maintenance. We thank Yulia Kagan for her help with the western blot.

Funding: Israel Science Foundation grant number 211/20 (S.B.D.), and Zuckerman fellowship (M.R.W.), TUD internal funding (YP). ANATOMIX is an Equipment of Excellence (EQUIPEX) funded by the Investments for the Future program of the French National Research Agency (ANR), project NanoimagesX, grant no. ANR-11-EQPX-0031. Access to ANATOMIX beamline is granted for proposal number proposal 20200811.

596

Figures

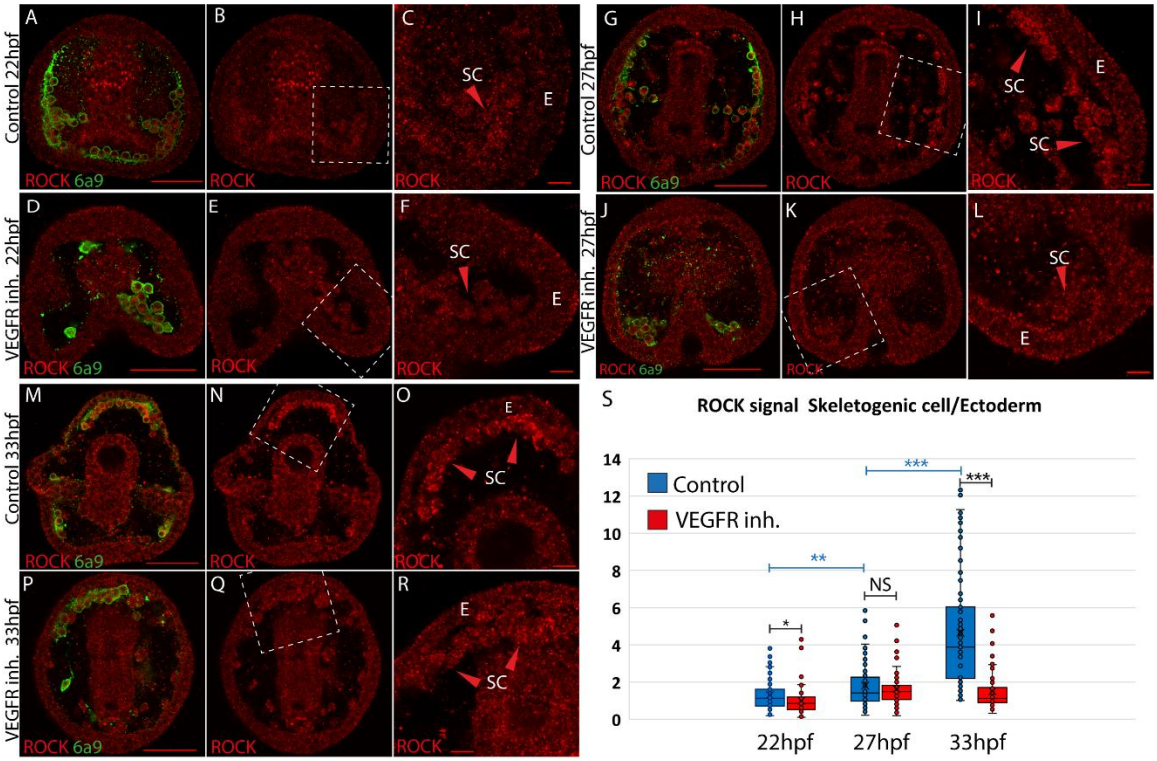

Figure 1 ROCK enrichment in the skeletogenic cells increases with time and depends on VEGF signaling. A-R, ROCK immunostaining at different times points in control and under VEGFR inhibition. In each condition and time point, the left image shows ROCK immunostaining and the skeletogenic cell marker, 6a9 (A, D, G, J, M and P). The middle image shows ROCK immunostaining alone in the whole embryo (B, E, H, K, N and Q). The right image shows the enlargement of the white rectangle region of the middle image (C, F, I, L, O, R). Scale bar in whole embryo is 50µm and in enlargements is 10µm. E – ectoderm, SC – skeletogenic cells. S, quantification of the ratio between ROCK signal/area in the skeletogenic cells compared to the ectodermal cells (see methods for details). Each box plot shows the average marked in x, the median, the first and the third quartiles (edges of boxes) and all experimental measurement (dots). Experiments were performed in three independent biological replicates and in each condition at least 33 embryos were measured. Statistical significance was measured using paired 2-tailed t-test where, * indicates $P<0.05$, ** indicates $P<0.005$, and *** indicates $P<0.0005$. The average ratios and ztest for significance difference from 1, are 22hpf control ~1.3, z=0.0006; VEGFR inhibition ~1, z=0.5, 27hpf control ~1.8, $z<10^{-11}$; VEGFR inhibition ~1.6, $z<10^{-8}$, 33hpf control ~4.6, $z<10^{-23}$; VEGFR inhibition ~1.5, $z<10^{-5}$.

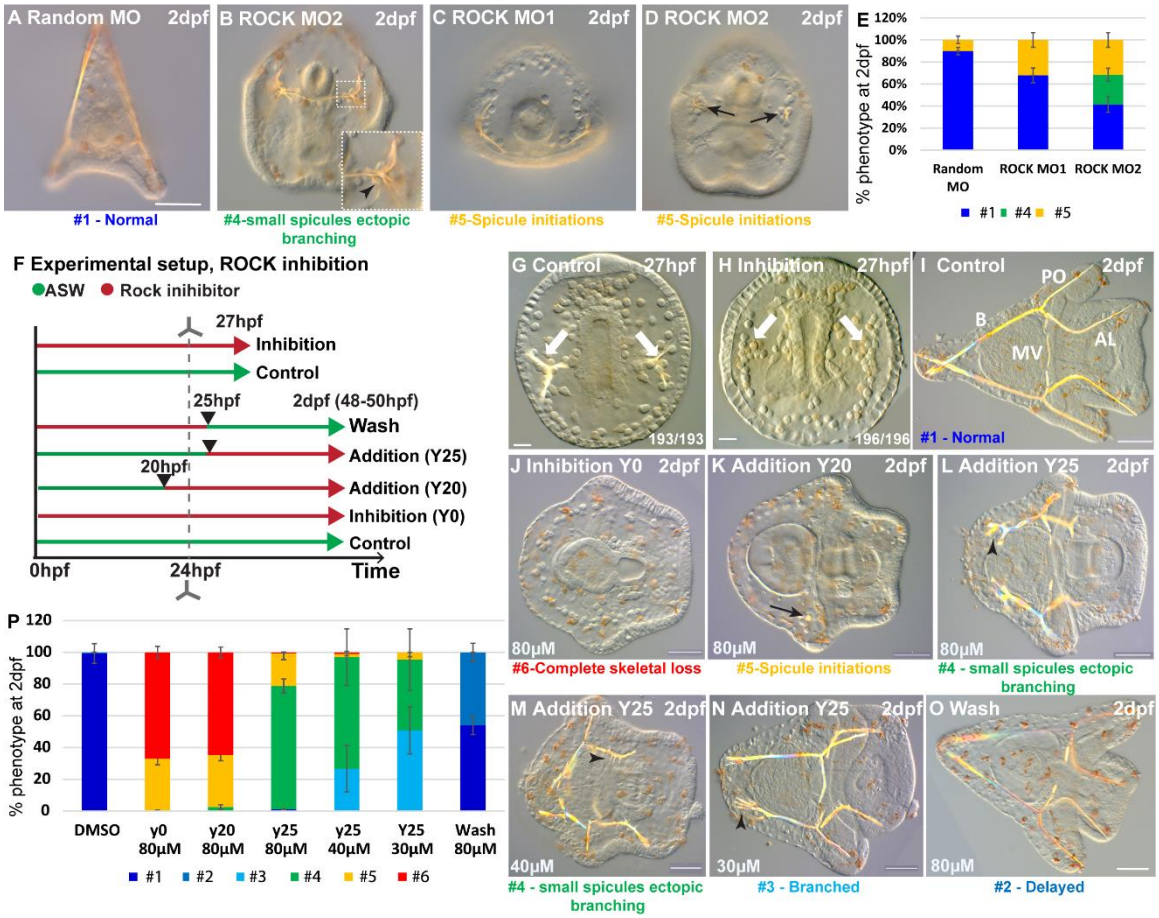

Figure 2 ROCK activity is essential for spicule formation and for normal elongation and branching morphology. A-E, genetic perturbation of ROCK translation using two different MASOs observed at 2dpf. A, control embryo injected with Random MASO develops normal skeleton. B, embryo injected with ROCK MO-2 shows ectopic spicule branching. C, D, embryos injected with ROCK MO-1 or MO-2 show spicule initiations. E, summary of MASO injection phenotypes based on 4-6 independent biological replicates, exact numbers are provided in Table S1. F-O, Pharmacological perturbations of ROCK activity using the inhibitor Y27632. F, experimental design of the various ROCK treatments showing the time of inhibitor addition/wash. G, Representative control embryo and H, embryo under ROCK inhibition using 80µM Y27632 at 27hpf. Results are based on four biological replicates and number of scored embryos that show the reported phenotype out of all embryos scored is indicated at the bottom of G and H. I-O, various skeletogenic phenotypes due to ROCK inhibition at different times and concentrations, observed at 2dpf. Treatment and concentrations are indicated for each image. I, the skeletal rods in control embryo are B, body; AL, anterolateral; PO, post-oral and MV, midventral. P, summary of ROCK perturbation phenotypes at 2dpf. Color codes of phenotypes match the color of the phenotypes reported in I-O. Results are based on 3-8 biological replicates for the different treatments, exact number of replicates and embryo scores for each experiment is provided in Table S1.

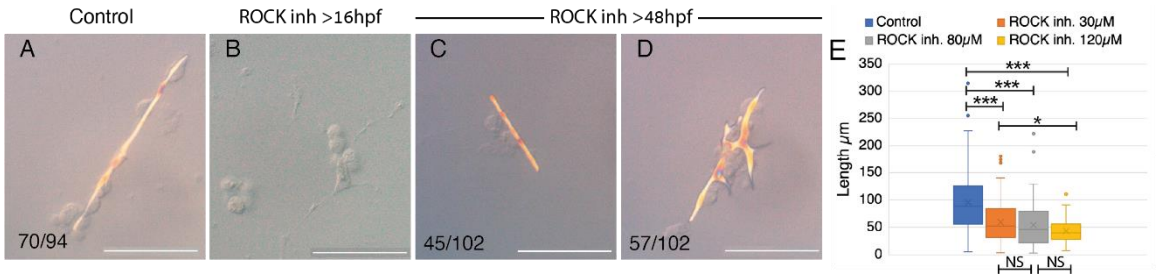

Figure 3 ROCK activity in the skeletogenic cells, *in-vitro*, is necessary for spicule formation, normal elongation and inhibition of branching. A-D, representative skeletogenic cell cultures at 72hpf. A, Linear skeletal rod in control skeletogenic cell culture. B-D, Inhibition of ROCK activity with 30µM Y27632. B, Inhibition of ROCK activity before spicule formation (at 16hpf) completely blocks spiculogenesis. C, Addition of ROCK inhibitor after spicule initiation, at 48hpf, reduces spicule elongation. D, spicule rod in ROCK inhibited skeletogenic cell culture shows branched phenotype. Scale bars represent 50µm. The numbers at the bottom indicate the number of spicules that show this phenotypes (left) over all observed spicules (right). E, Quantification of spicule length in control and ROCK inhibited skeletogenic cell culture (inhibitor added at 48hpf) at 72hpf. Each box plot shows an average, the first and the third quartiles (edges of boxes) and outliers (dots). Statistical analysis was performed using Kruskal-Wallis non-parametric test. Results are based on three biological repeats for each treatment, except from 120µm that was done in two biological repeats. The exact number of studied skeletons can be found in material & methods. Kruskal-Wallis; statistical significance is represented by *P < 0.05, ***P < 0.0001.

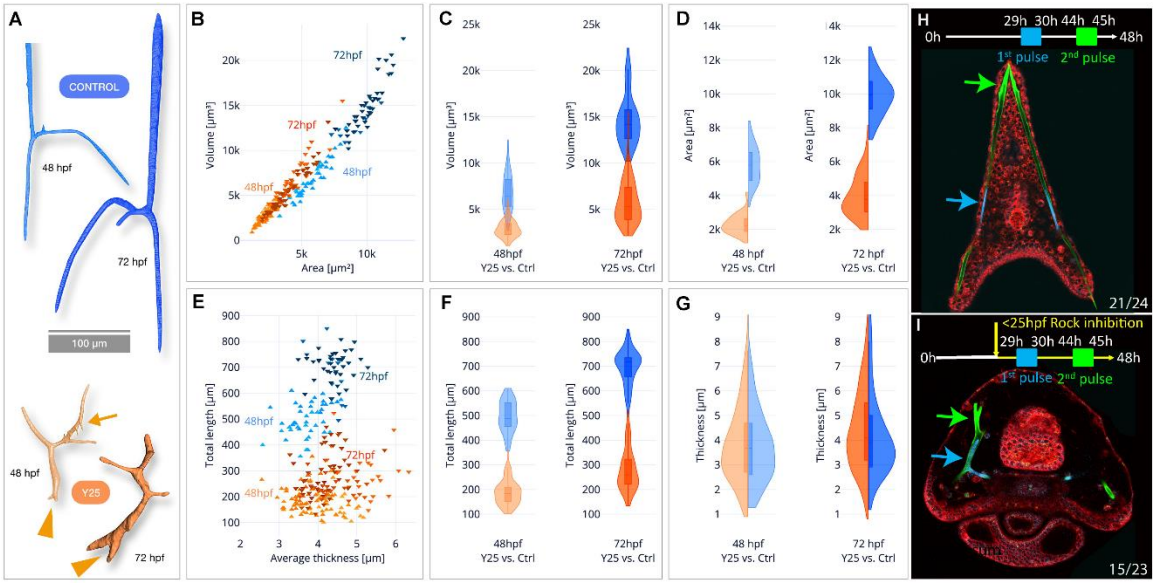

Figure 4 SR-µCT studies of ROCK inhibited spicuels show reduction in skeletal volume, surface area and total length, but not thickness and 2-pulse calcein shows loss of tip-dominance. A, Exemplary 3D-renderings of control spicules (top, blue) and spicules where 40µM of ROCK inhibitor was added at 25hpf (bottom, orange), dissected at 48hpf and 72hpf. Arrowheads point to tip splitting and arrow at 48hpf point to spicule dripping at the back. B, Spicule volume vs. area for control and ROCK-inhibited spicules at 48 and 72 hpf. Each data point represents a single spicule. C-D, Frequency distributions for volume and surface area of control and ROCK-inhibited spicules at 48 hpf and 72 hpf (left and right violin plots, respectively). E, Spicules' total branch length and average thickness for control and ROCK-inhibited spicules at 48 and 72 hpf. F-G, Frequency distributions for spicule lengths and thickness of control and ROCK-inhibited spicules dissected at 48hpf and 72hpf (left and right violin plots, respectively). H, I, Calcein two-pulses experiment shows loss of tip-dominance under ROCK inhibition. Embryos were exposed to blue calcein from 29-30hpf, and to green calcein from 44-45hpf. Embryos were stained with FM4-64 membrane marker (red) prior to image acquisition at 48hpf. H, Control embryo, G, Embryo where 30µM of Y27632 was added at 25hpf. The experiments were done in three biological replicates and the numbers at the bottom indicate the number of embryos that show this phenotype out of all embryos scored.

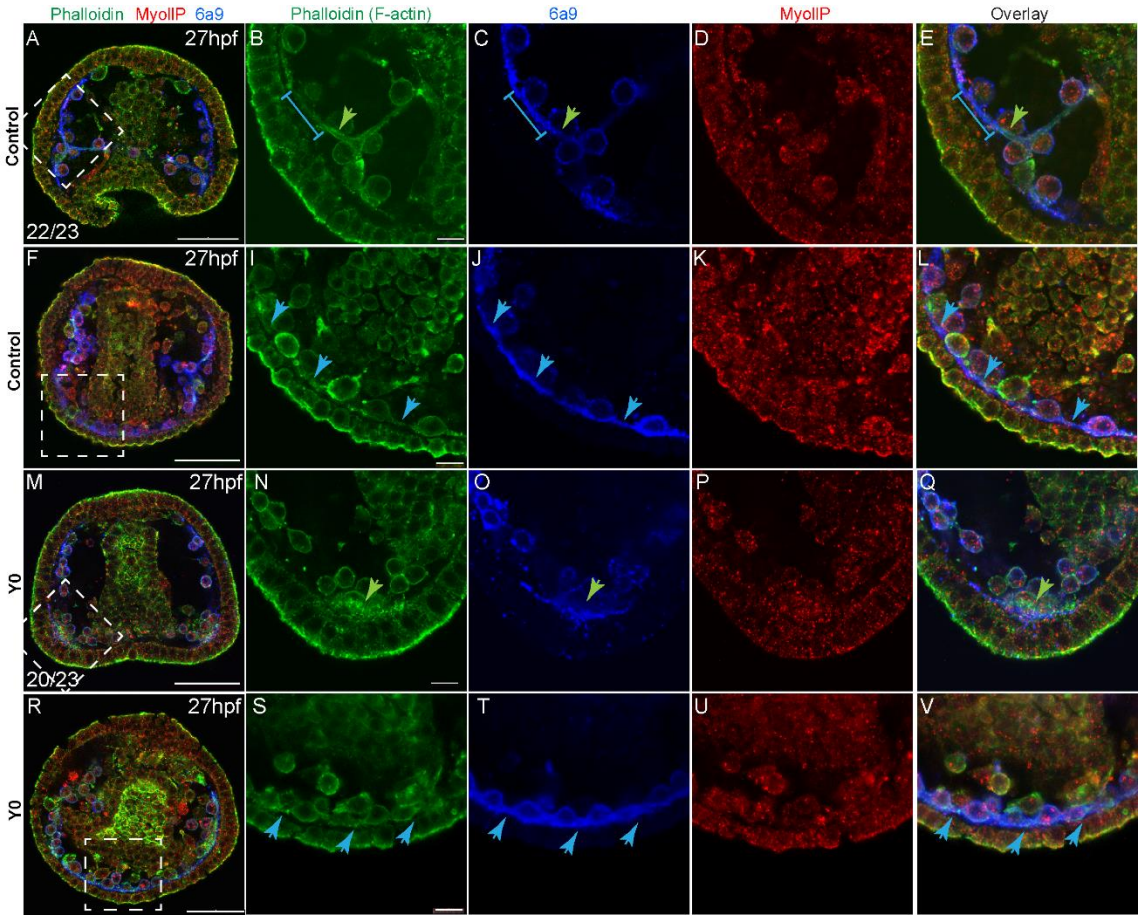

Figure 5 ROCK inhibition interferes with F-actin organization around the spicule but the pseudopodia cable between the skeletogenic cells still forms. Representative images showing normal embryo (A-L) and embryos treated with ROCK inhibitor from fertilization (M-V, 80μM), at 27hpf. Phalloidin (green) was used to stain F-actin, MyoIIP (red) was used to stain phosphorylated myosinII and 6a9 (blue) was used to mark the skeletogenic cells. Right panels show enlargements of the rectangle sections marked in the left most panels. Green arrows point to regions that show enriched F-actin signal, blue arrows point to the pseudopodia cable. The blue line in B, C and E marks a region of the pseudopodia cable that is stained by 6a9 but has low F-actin signal. The experiments were done in 3 biological replicates, the numbers at the bottom left of (A, M) indicate the number of embryos that show this phenotype out of all embryos scored. Scale bar in A, F, M and R is 50μm, and in B, I, N and S is 10μm.

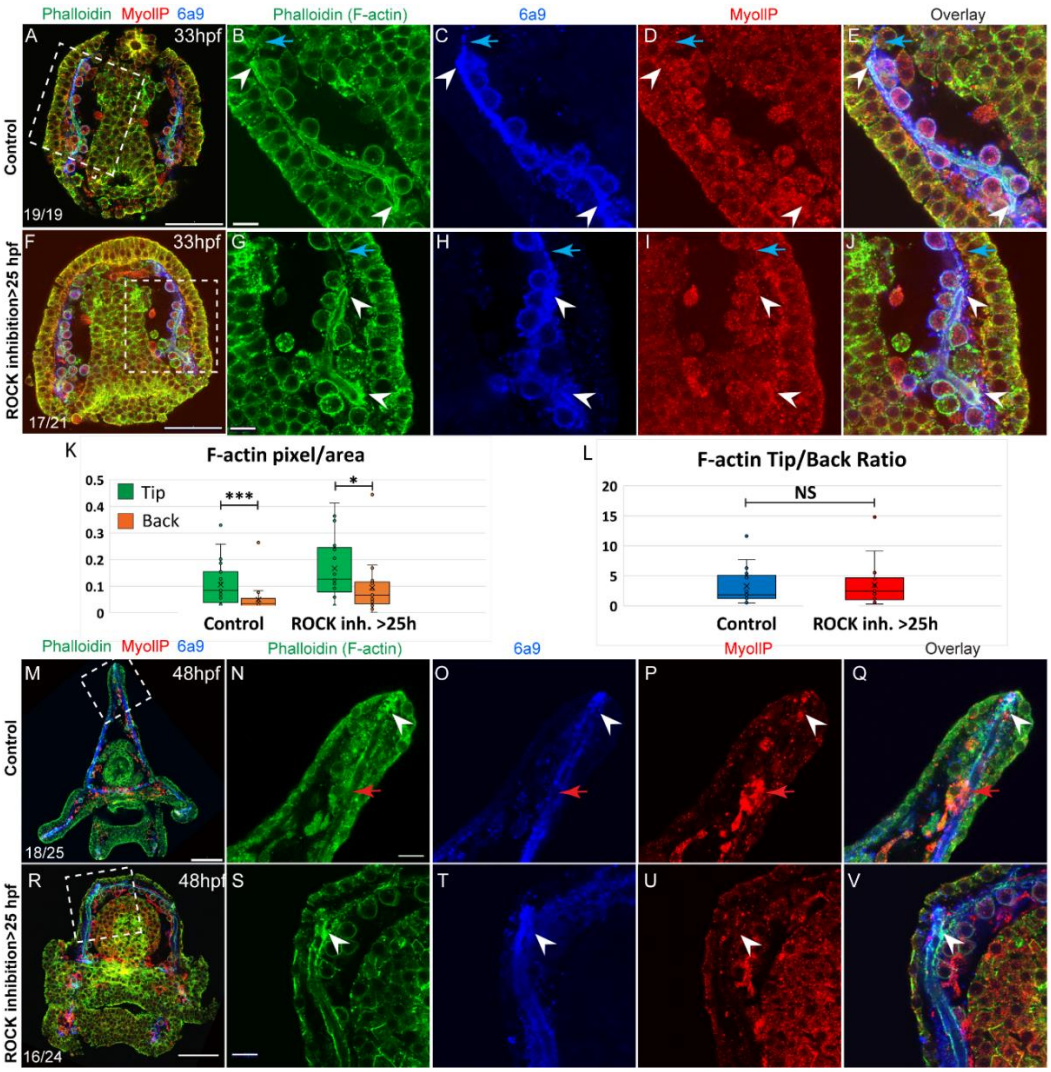

Figure 6 During skeletal elongation F-actin filaments are enriched at the tips of the rods independently on ROCK Activity. A-J, representative images at 33hpf, showing normal embryo (A-E) and embryos treated with ROCK inhibitor from the gastrula stage (>25hpf, 30µM, F-J). Embryos are stained with Phalloidin (green), MyollP antibody (red) and 6a9 (blue). B-E, G-J, enlargement sections of the spicule area marked with rectangle in A and G. White arrowheads point to the enriched F-actin signal at the tips. Blue arrows point to the region of the pseudopodia cable that is not filled with the spicule cavity. K, L, quantification of the tip to back F-actin signal (number of green pixels per area) at 33hpf in control embryos and ROCK inhibition >25hpf. Each box plot shows the average (x), median (middle line), the first and the third quartiles and all the points measured. Asterisks indicate statistical significance in paired t-test, where * is $p<0.05$ and *** is $p< 0.0005$, NS- not significant. M-V, similar experiments to A-J, at 48hpf, 40µM of ROCK inhibitor added at 25hpf. Red arrows point to non-skeletogenic cells enriched with MyoIIP. The experiments were repeated in 3 biological replicates and the numbers at the bottom left of (A, F, M, R) indicate the number of embryos that show this phenotype out of all embryos scored. Scale bar in A, F, M, R is 50µm and in B, G, N, S, is 10µm.

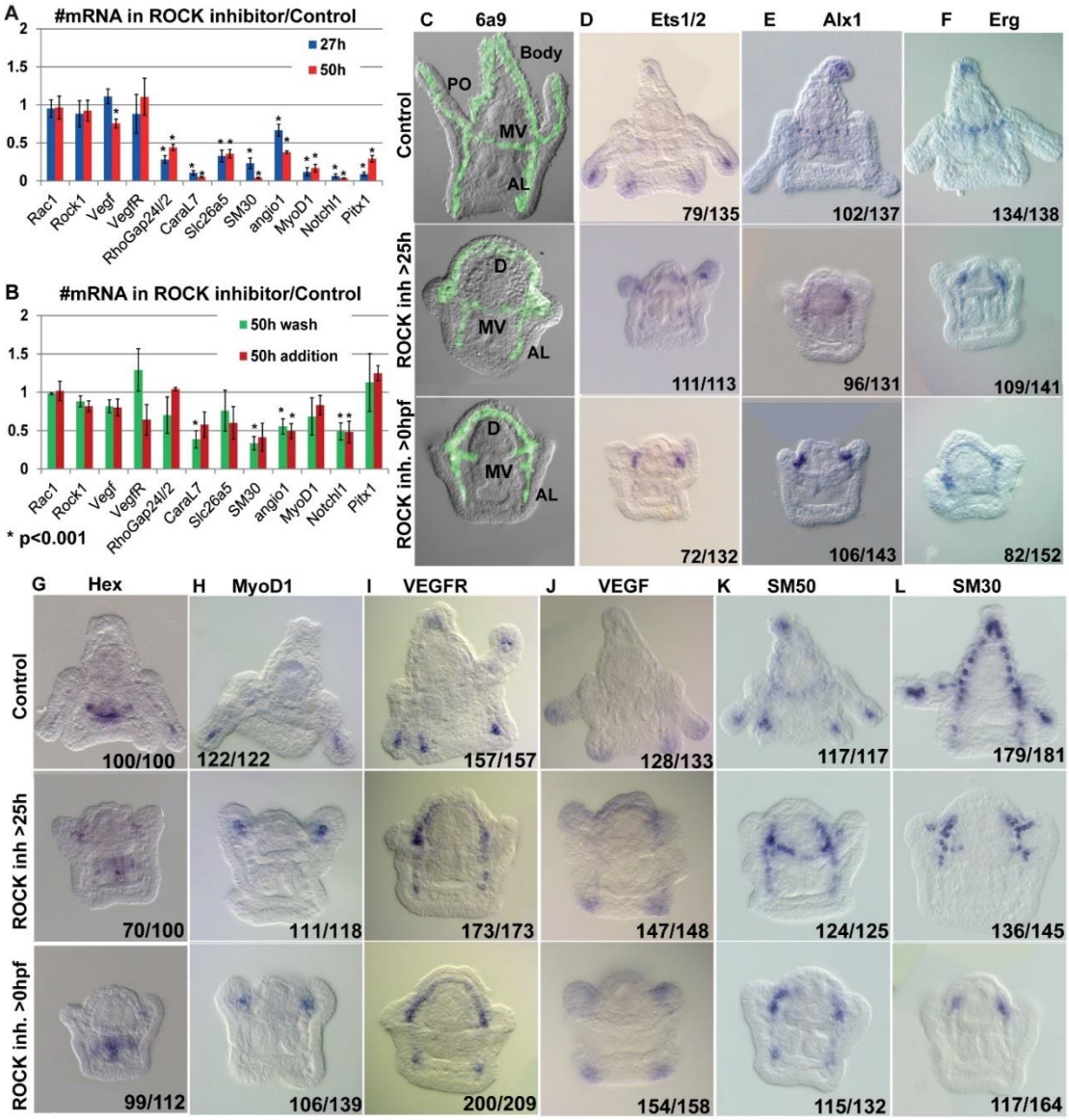

Figure 7 ROCK activity is essential for normal gene expression in the skeletogenic cells. (A) the effect of continuous ROCK inhibition on gene expression levels at 27hpf and 50hpf. (B) the effect of the addition of ROCK inhibitor at 25hpf and the wash of ROCK inhibitor at 25hpf, on gene expression level measured at 50hpf. Inhibitor concentration is 80µM and the QPCR experiments are based on 4 biological replicates in (A) and 3 in (B) Asterisks indicate $p<0.001$, one tailed z-test. Error bars show standard deviation. (C-L) Representative images of control embryo (top panels), embryos where ROCK inhibitor was added at 25hpf (middle panels), and embryos that were exposed to continuous ROCK inhibition (bottom panels), at the pluteus stage (~48hpf). (C) skeletogenic cell marker, 6a9. MV, midventral; AL, anterolateral, and PO, Post-oral rods, D, dorsal skeletogenic chain. (D-L) spatial expression of skeletogenic genes. Gene names are indicated at the top of each panel. Numbers at the bottom of each image indicate the number of embryos that show this phenotype (left) out of all embryos scored (right), conducted in at least three independent biological replicates.

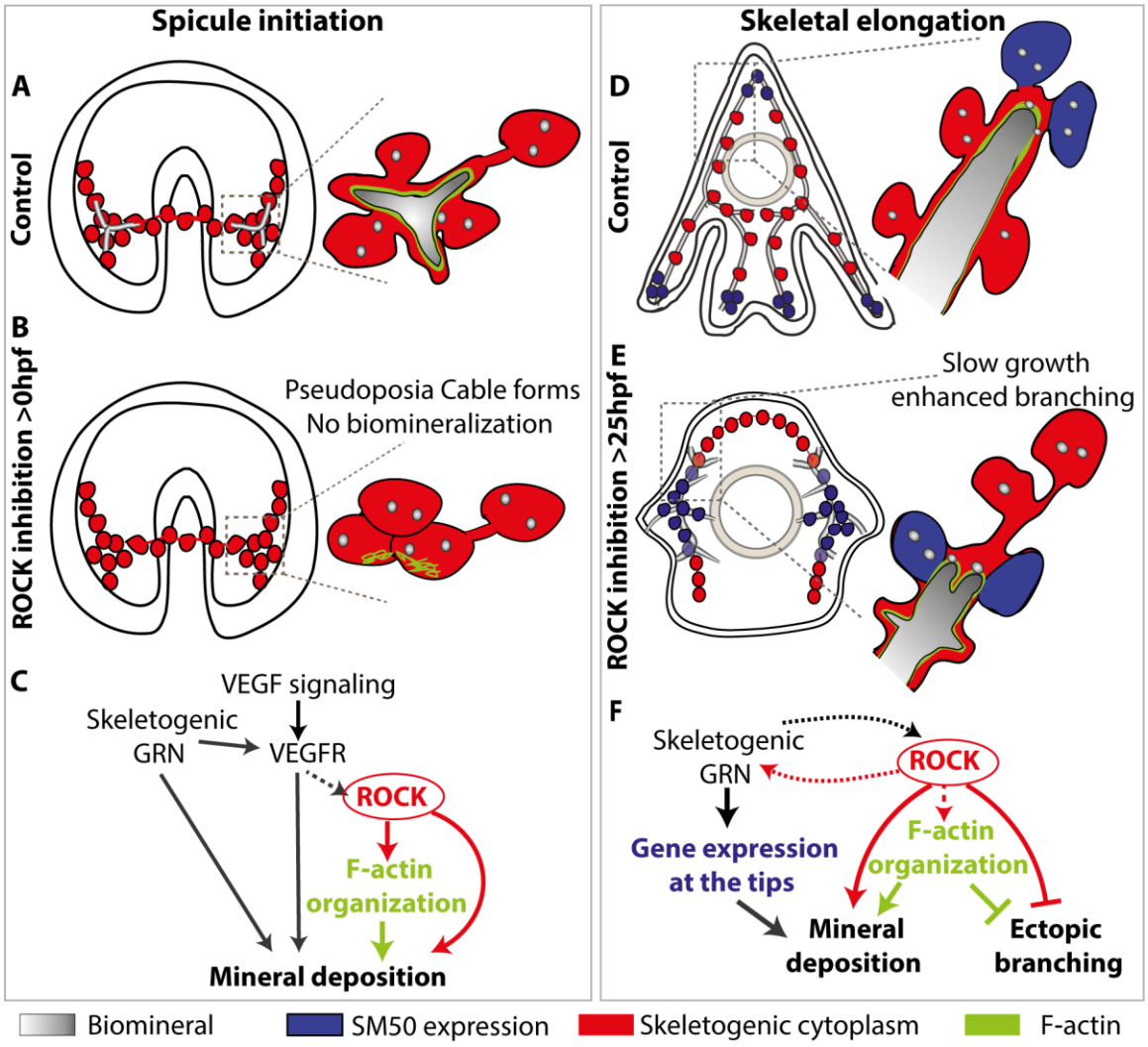

Figure 8 A model of ROCK regulation of spicule formation and elongation. A, B, at the gastrula stage (~27hpf in *P. lividus*), the triradiate spicule is coated with F-actin in normal embryos (A). ROCK continuous inhibition prevents spicule formation. F-actin enrichment is detected in the skeletogenic cells at the lateral clusters but is not organized. C, a model of the regulation and activity of ROCK and F-actin during the first stages of spicule initiation (~24-27hpf in *P. lividus*). VEGF signaling is required for the early skeletogenic cell migration and for the enrichment of ROCK in the skeletogenic cells. ROCK activity is required for spicule initiation and for F-actin organization around the spicules. D, during skeletal elongation F-actin is detected around the spicule cavity and is enriched at the tips of the rods. The expression of SM50 and some other skeletogenic genes, is localized to the tips of the rods. D, under the addition of ROCK inhibitor, skeletal growth rate is reduced and ectopic spicule branching is observed. The expression of skeletogenic genes is localized to the vicinity of the growing rods and does not progress to the edges of the dorsal and anterolateral chains. F, a model of the regulation and activity of ROCK and F-actin during skeletal elongation.

References

1. Evans JS. The Biomineralization Proteome: Protein Complexity for a Complex Bioceramic Assembly Process. Proteomics. 2019;19(16):e1900036. Epub 2019/06/21. doi: 10.1002/pmic.201900036. PubMed PMID: 31219243.
2. Weiner S, Addadi I. Crystallization Pathways in Biomineralization. Annu Rev Mater Res. 2011;41:21-40.
3. Ben-Tabou de-Leon S. The Evolution of Biomineralization through the Co-Option of Organic Scaffold Forming Networks. Cells. 2022;11(4). Epub 20220209. doi: 10.3390/cells11040595. PubMed PMID: 35203246; PubMed Central PMCID: PMCPMC8870065.
4. Morgulis M, Gildor T, Roopin M, Sher N, Malik A, Lalzar M, et al. Possible cooption of a VEGF-driven tubulogenesis program for biomineralization in echinoderms. Proc Natl Acad Sci U S A. 2019;116(25):12353-62. Epub 2019/06/04. doi: 10.1073/pnas.1902126116. PubMed PMID: 31152134; PubMed Central PMCID: PMCPMC6589685.
5. Murdock DJE. The 'biomineralization toolkit' and the origin of animal skeletons. Biol Rev Camb Philos Soc. 2020;95(5):1372-92. Epub 2020/05/25. doi: 10.1111/brv.12614. PubMed PMID: 32447836.
6. Murdock DJ, Donoghue PC. Evolutionary origins of animal skeletal biomineralization. Cells Tissues Organs. 2011;194(2-4):98-102. Epub 2011/06/01. doi: 10.1159/000324245. PubMed PMID: 21625061.
7. Knoll AH. Biomineralization and Evolutionary History. Reviews in Mineralogy and Geochemistry. 2003;54:329-56. doi: doi:10.2113/0540329.
8. Gilbert P, Bergmann KD, Boekelheide N, Tambutte S, Mass T, Marin F, et al. Biomineralization: Integrating mechanism and evolutionary history. Sci Adv. 2022;8(10):eabl9653. Epub 20220309. doi: 10.1126/sciadv.abl9653. PubMed PMID: 35263127; PubMed Central PMCID: PMCPMC8906573.
9. Hojo H, McMahon AP, Ohba S. An Emerging Regulatory Landscape for Skeletal Development. Trends Genet. 2016;32(12):774-87. Epub 2016/11/07. doi: 10.1016/j.tig.2016.10.001. PubMed PMID: 27814929; PubMed Central PMCID: PMCPMC5126973.
10. Khor JM, Ettensohn CA. Functional divergence of paralogous transcription factors supported the evolution of biomineralization in echinoderms. eLife. 2017;6. Epub 2017/11/21. doi: 10.7554/eLife.32728. PubMed PMID: 29154754; PubMed Central PMCID: PMCPMC5758115.
11. Fraser GJ, Hulsey CD, Bloomquist RF, Uyesugi K, Manley NR, Streelman JT. An ancient gene network is co-opted for teeth on old and new jaws. PLoS Biol. 2009;7(2):e31. Epub 2009/02/14. doi: 08-PLBI-RA-2652 [pii]

10.1371/journal.pbio.1000031. PubMed PMID: 19215146; PubMed Central PMCID: PMC2637924.
12. Gotliv BA, Addadi L, Weiner S. Mollusk shell acidic proteins: in search of individual functions. Chembiochem : a European journal of chemical biology. 2003;4(6):522-9. Epub 2003/06/10. doi: 10.1002/cbic.200200548. PubMed PMID: 12794863.
13. Gong YU, Killian CE, Olson IC, Appathurai NP, Amasino AL, Martin MC, et al. Phase transitions in biogenic amorphous calcium carbonate. Proc Natl Acad Sci U S A. 2012;109(16):6088-93. Epub 2012/04/12. doi: 10.1073/pnas.1118085109. PubMed PMID: 22492931; PubMed Central PMCID: PMC3341025.

785 14. Kawasaki K, Buchanan AV, Weiss KM. Biomineralization in humans: making the hard
786 choices in life. Annu Rev Genet. 2009;43:119-42. Epub 2009/08/08. doi: 10.1146/annurev-genet-
787 102108-134242. PubMed PMID: 19659443.
788 15. Drake JL, Mass T, Haramaty L, Zelzion E, Bhattacharya D, Falkowski PG. Proteomic
789 analysis of skeletal organic matrix from the stony coral Stylophora pistillata. Proc Natl Acad Sci U
790 S A. 2013;110(10):3788-93. Epub 2013/02/23. doi: 10.1073/pnas.1301419110. PubMed PMID:
791 23431140; PubMed Central PMCID: PMCPMC3593878.
792 16. Tucker A, Sharpe P. The cutting-edge of mammalian development; how the embryo
793 makes teeth. Nat Rev Genet. 2004;5(7):499-508. doi: 10.1038/nrg1380. PubMed PMID:
794 15211352.
795 17. Langer G, Jan de Nooijer L, Oetjen K. On the role of cytoskeleton in coccolith
796 morphogenesis: the effect of cytoskeleton inhibitors. Journal of Phycology. 2010;46:1252–6. doi:
797 DOI: 10.1111/j.1529-8817.2010.00916.x.
798 18. Durak GM, Brownlee C, Wheeler GL. The role of the cytoskeleton in biomineralisation in
799 haptophyte algae. Scientific reports. 2017;7(1):15409. Epub 2017/11/15. doi: 10.1038/s41598-
800 017-15562-8. PubMed PMID: 29133928; PubMed Central PMCID: PMCPMC5684398.
801 19. Tyszka J, Bickmeyer U, Raitzsch M, Bijma J, Kaczmarek K, Mewes A, et al. Form and
802 function of F-actin during biomineralization revealed from live experiments on foraminifera.
803 Proc Natl Acad Sci U S A. 2019;116(10):4111-6. Epub 2019/02/21. doi:
804 10.1073/pnas.1810394116. PubMed PMID: 30782789; PubMed Central PMCID:
805 PMCPMC6410838.
806 20. Tesson B, Hildebrand M. Dynamics of silica cell wall morphogenesis in the diatom
807 Cyclotella cryptica: substructure formation and the role of microfilaments. J Struct Biol.
808 2010;169(1):62-74. Epub 2009/09/05. doi: 10.1016/j.jsb.2009.08.013. PubMed PMID: 19729066.
809 21. Tesson B, Hildebrand M. Extensive and intimate association of the cytoskeleton with
810 forming silica in diatoms: control over patterning on the meso- and micro-scale. PLoS One.
811 2010;5(12):e14300. Epub 2011/01/05. doi: 10.1371/journal.pone.0014300. PubMed PMID:
812 21200414; PubMed Central PMCID: PMCPMC3000822.
813 22. Strzelecka-Kiliszek A, Mebarek S, Roszkowska M, Buchet R, Magne D, Pikula S. Functions
814 of Rho family of small GTPases and Rho-associated coiled-coil kinases in bone cells during
815 differentiation and mineralization. Biochim Biophys Acta Gen Subj. 2017;1861(5 Pt A):1009-23.
816 Epub 20170208. doi: 10.1016/j.bbagen.2017.02.005. PubMed PMID: 28188861.
817 23. Qin L, Liu W, Cao H, Xiao G. Molecular mechanosensors in osteocytes. Bone Res.
818 2020;8:23. Epub 20200608. doi: 10.1038/s41413-020-0099-y. PubMed PMID: 32550039;
819 PubMed Central PMCID: PMCPMC7280204.
820 24. Huang X, Chen X, Chen H, Xu D, Lin C, Peng B. Rho/Rho-associated protein kinase
821 signaling pathway-mediated downregulation of runt-related transcription factor 2 expression
822 promotes the differentiation of dental pulp stem cells into odontoblasts. Exp Ther Med.
823 2018;15(5):4457-64. Epub 20180321. doi: 10.3892/etm.2018.5982. PubMed PMID: 29731830;
824 PubMed Central PMCID: PMCPMC5920824.
825 25. Lecuit T, Lenne PF, Munro E. Force generation, transmission, and integration during cell
826 and tissue morphogenesis. Annu Rev Cell Dev Biol. 2011;27:157-84. Epub 2011/07/12. doi:
827 10.1146/annurev-cellbio-100109-104027. PubMed PMID: 21740231.
828 26. Munjal A, Lecuit T. Actomyosin networks and tissue morphogenesis. Development.
829 2014;141(9):1789-93. Epub 2014/04/24. doi: 10.1242/dev.091645. PubMed PMID: 24757001.
830 27. Agarwal P, Zaidel-Bar R. Principles of Actomyosin Regulation In Vivo. Trends Cell Biol.
831 2019;29(2):150-63. Epub 2018/11/06. doi: 10.1016/j.tcb.2018.09.006. PubMed PMID:
832 30385150.

833 28. Raftopoulou M, Hall A. Cell migration: Rho GTPases lead the way. Dev Biol.
834 2004;265(1):23-32. doi: 10.1016/j.ydbio.2003.06.003. PubMed PMID: 14697350.
835 29. Miklavc P, Frick M. Actin and Myosin in Non-Neuronal Exocytosis. Cells. 2020;9(6). Epub
836 20200611. doi: 10.3390/cells9061455. PubMed PMID: 32545391; PubMed Central PMCID:
837 PMCPMC7348895.
838 30. Segal D, Zaritsky A, Schejter ED, Shilo BZ. Feedback inhibition of actin on Rho mediates
839 content release from large secretory vesicles. J Cell Biol. 2018;217(5):1815-26. Epub
840 2018/03/03. doi: 10.1083/jcb.201711006. PubMed PMID: 29496739; PubMed Central PMCID:
841 PMCPMC5940311.
842 31. Rousso T, Schejter ED, Shilo BZ. Orchestrated content release from Drosophila glue-
843 protein vesicles by a contractile actomyosin network. Nat Cell Biol. 2016;18(2):181-90. Epub
844 2015/12/08. doi: 10.1038/ncb3288. PubMed PMID: 26641716.
845 32. Oliveri P, Tu Q, Davidson EH. Global regulatory logic for specification of an embryonic
846 cell lineage. Proc Natl Acad Sci U S A. 2008;105(16):5955-62. Epub 2008/04/17. doi:
847 10.1073/pnas.0711220105. PubMed PMID: 18413610; PubMed Central PMCID: PMC2329687.
848 33. Ettensohn CA, Dey D. KirrelL, a member of the Ig-domain superfamily of adhesion
849 proteins, is essential for fusion of primary mesenchyme cells in the sea urchin embryo. Dev Biol.
850 2017;421(2):258-70. doi: 10.1016/j.ydbio.2016.11.006. PubMed PMID: 27866905.
851 34. Gildor T, Winter MR, Layous M, Hijaze E, Ben-Tabou de-Leon S. The biological regulation
852 of sea urchin larval skeletogenesis - From genes to biomineralized tissue. J Struct Biol.
853 2021:107797. Epub 2021/09/17. doi: 10.1016/j.jsb.2021.107797. PubMed PMID: 34530133.
854 35. Kahil K, Varsano N, Sorrentino A, Pereiro E, Rez P, Weiner S, et al. Cellular pathways of
855 calcium transport and concentration toward mineral formation in sea urchin larvae. Proc Natl
856 Acad Sci U S A. 2020;117(49):30957-65. Epub 2020/11/25. doi: 10.1073/pnas.1918195117.
857 PubMed PMID: 33229583; PubMed Central PMCID: PMCPMC7733801.
858 36. Vidavsky N, Addadi S, Mahamid J, Shimoni E, Ben-Ezra D, Shpigel M, et al. Initial stages
859 of calcium uptake and mineral deposition in sea urchin embryos. Proc Natl Acad Sci U S A.
860 2014;111(1):39-44. Epub 2013/12/18. doi: 10.1073/pnas.1312833110. PubMed PMID:
861 24344263; PubMed Central PMCID: PMC3890786.
862 37. Wilt FH, Killian CE, Hamilton P, Croker L. The dynamics of secretion during sea urchin
863 embryonic skeleton formation. Exp Cell Res. 2008;314(8):1744-52. Epub 2008/03/22. doi:
864 10.1016/j.yexcr.2008.01.036. PubMed PMID: 18355808; PubMed Central PMCID: PMC2444014.
865 38. Adomako-Ankomah A, Ettensohn CA. Growth factor-mediated mesodermal cell
866 guidance and skeletogenesis during sea urchin gastrulation. Development. 2013;140(20):4214-
867 25. doi: 10.1242/dev.100479. PubMed PMID: 24026121.
868 39. Morgulis M, Gildor T, Roopin M, Sher N, Malik A, Lalzar M, et al. Possible cooption of a
869 VEGF-driven tubulogenesis program for biomineralization in echinoderms. Proc Natl Acad Sci U S
870 A. 2019. doi: 10.1073/pnas.1902126116. PubMed PMID: 31152134.
871 40. Sun Z, Ettensohn CA. Signal-dependent regulation of the sea urchin skeletogenic gene
872 regulatory network. Gene Expr Patterns. 2014;16(2):93-103. doi: 10.1016/j.gep.2014.10.002.
873 PubMed PMID: 25460514.
874 41. Tarsis K, Gildor T, Morgulis M, Ben-Tabou de-Leon S. Distinct regulatory states control
875 the elongation of individual skeletal rods in the sea urchin embryo. Dev Dyn. 2022. Epub
876 20220410. doi: 10.1002/dvdy.474. PubMed PMID: 35403290.
877 42. Morgulis M, Winter MR, Shternhell L, Gildor T, Ben-Tabou de-Leon S. VEGF signaling
878 activates the matrix metalloproteinases, MmpL7 and MmpL5 at the sites of active skeletal
879 growth and MmpL7 regulates skeletal elongation. Dev Biol. 2021;473:80-9. Epub 2021/02/13.
880 doi: 10.1016/j.ydbio.2021.01.013. PubMed PMID: 33577829.

881 43. Winter MR, Morgulis M, Gildor T, Cohen AR, Ben-Tabou de-Leon S. Calcium-vesicles
882 perform active diffusion in the sea urchin embryo during larval biomineralization. PLoS Comput
883 Biol. 2021;17(2):e1008780. Epub 2021/02/23. doi: 10.1371/journal.pcbi.1008780. PubMed
884 PMID: 33617532; PubMed Central PMCID: PMCPMC7932551.
885 44. Stepicheva NA, Dumas M, Kobi P, Donaldson JG, Song JL. The small GTPase Arf6
886 regulates sea urchin morphogenesis. Differentiation. 2017;95:31-43. doi:
887 10.1016/j.diff.2017.01.003. PubMed PMID: 28188999.
888 45. Moreno B, DiCorato A, Park A, Kellen Mobilia, Knapp R, Bleher R, et al. Culture of and
889 experiments with sea urchin embryo primary mesenchyme cells. Methods in Cell Biology.
890 2019;150:293-330.
891 46. Sepulveda-Ramirez SP, Toledo-Jacobo L, Henson JH, Shuster CB. Cdc42 controls primary
892 mesenchyme cell morphogenesis in the sea urchin embryo. Dev Biol. 2018;437(2):140-51. Epub
893 2018/03/21. doi: 10.1016/j.ydbio.2018.03.015. PubMed PMID: 29555242; PubMed Central
894 PMCID: PMCPMC5973877.
895 47. Croce J, Duloquin L, Lhomond G, McClay DR, Gache C. Frizzled5/8 is required in
896 secondary mesenchyme cells to initiate archenteron invagination during sea urchin
897 development. Development. 2006;133(3):547-57. doi: 10.1242/dev.02218. PubMed PMID:
898 16396908.
899 48. Ettensohn CA, McClay DR. Cell lineage conversion in the sea urchin embryo. Dev Biol.
900 1988;125(2):396-409. Epub 1988/02/01. doi: 10.1016/0012-1606(88)90220-5. PubMed PMID:
901 3338620.
902 49. Chen W, Mao K, Liu Z, Dinh-Xuan AT. The role of the RhoA/Rho kinase pathway in
903 angiogenesis and its potential value in prostate cancer (Review). Oncol Lett. 2014;8(5):1907-11.
904 Epub 20140821. doi: 10.3892/ol.2014.2471. PubMed PMID: 25289078; PubMed Central PMCID:
905 PMCPMC4186560.
906 50. Jacobs M, Hayakawa K, Swenson L, Bellon S, Fleming M, Taslimi P, et al. The structure of
907 dimeric ROCK I reveals the mechanism for ligand selectivity. J Biol Chem. 2006;281(1):260-8. doi:
908 10.1074/jbc.M508847200. PubMed PMID: 16249185.
909 51. Liu J, Wada Y, Katsura M, Tozawa H, Erwin N, Kapron CM, et al. Rho-Associated Coiled-
910 Coil Kinase (ROCK) in Molecular Regulation of Angiogenesis. Theranostics. 2018;8(21):6053-69.
911 Epub 2019/01/08. doi: 10.7150/thno.30305. PubMed PMID: 30613282; PubMed Central PMCID:
912 PMCPMC6299434.
913 52. Julian L, Olson MF. Rho-associated coiled-coil containing kinases (ROCK): structure,
914 regulation, and functions. Small GTPases. 2014;5:e29846. Epub 2014/07/11. doi:
915 10.4161/sgtp.29846. PubMed PMID: 25010901; PubMed Central PMCID: PMCPMC4114931.
916 53. Amin E, Dubey BN, Zhang SC, Gremer L, Dvorsky R, Moll JM, et al. Rho-kinase:
917 regulation, (dys)function, and inhibition. Biol Chem. 2013;394(11):1399-410. doi: 10.1515/hsz-
918 2013-0181. PubMed PMID: 23950574; PubMed Central PMCID: PMCPMC5538733.
919 54. Pavlov D, Muhlrad A, Cooper J, Wear M, Reisler E. Actin filament severing by cofilin. J
920 Mol Biol. 2007;365(5):1350-8. Epub 20061103. doi: 10.1016/j.jmb.2006.10.102. PubMed PMID:
921 17134718; PubMed Central PMCID: PMCPMC2572264.
922 55. Yarmola EG, Somasundaram T, Boring TA, Spector I, Bubb MR. Actin-latrunculin A
923 structure and function. Differential modulation of actin-binding protein function by latrunculin
924 A. J Biol Chem. 2000;275(36):28120-7. doi: 10.1074/jbc.M004253200. PubMed PMID: 10859320.
925 56. Schatten G, Schatten H, Spector I, Cline C, Paweletz N, Simerly C, et al. Latrunculin
926 inhibits the microfilament-mediated processes during fertilization, cleavage and early
927 development in sea urchins and mice. Exp Cell Res. 1986;166(1):191-208. doi: 10.1016/0014-
928 4827(86)90519-7. PubMed PMID: 3743654.

929 57. Kovacs M, Toth J, Hetenyi C, Malnasi-Csizmadia A, Sellers JR. Mechanism of blebbistatin
930 inhibition of myosin II. J Biol Chem. 2004;279(34):35557-63. Epub 20040616. doi:
931 10.1074/jbc.M405319200. PubMed PMID: 15205456.
932 58. Moorhouse KS, Gudejko HF, McDougall A, Burgess DR. Influence of cell polarity on early
933 development of the sea urchin embryo. Dev Dyn. 2015;244(12):1469-84. Epub 20150925. doi:
934 10.1002/dvdy.24337. PubMed PMID: 26293695; PubMed Central PMCID: PMCPMC4715636.
935 59. Mabuchi I. Cleavage furrow: timing of emergence of contractile ring actin filaments and
936 establishment of the contractile ring by filament bundling in sea urchin eggs. J Cell Sci. 1994;107
937 (Pt 7):1853-62. doi: 10.1242/jcs.107.7.1853. PubMed PMID: 7983152.
938 60. Schroeder TE. Fourth cleavage of sea urchin blastomeres: microtubule patterns and
939 myosin localization in equal and unequal cell divisions. Dev Biol. 1987;124(1):9-22. doi:
940 10.1016/0012-1606(87)90454-4. PubMed PMID: 3311851.
941 61. Wong GK, Allen PG, Begg DA. Dynamics of filamentous actin organization in the sea
942 urchin egg cortex during early cleavage divisions: implications for the mechanism of cytokinesis.
943 Cell motility and the cytoskeleton. 1997;36(1):30-42. doi: 10.1002/(SICI)1097-
944 0169(1997)36:1<30::AID-CM3>3.0.CO;2-L. PubMed PMID: 8986375.
945 62. Khor JM, Ettensohn CA. Transcription Factors of the Alx Family: Evolutionarily Conserved
946 Regulators of Deuterostome Skeletogenesis. Frontiers in genetics. 2020;11:569314. Epub
947 2020/12/18. doi: 10.3389/fgene.2020.569314. PubMed PMID: 33329706; PubMed Central
948 PMCID: PMCPMC7719703.
949 63. Bond LM, Brandstaetter H, Sellers JR, Kendrick-Jones J, Buss F. Myosin motor proteins
950 are involved in the final stages of the secretory pathways. Biochem Soc Trans. 2011;39(5):1115-
951 9. doi: 10.1042/BST0391115. PubMed PMID: 21936774; PubMed Central PMCID:
952 PMCPMC3403808.
953 64. Bibeau JP, Kingsley JL, Furt F, Tuzel E, Vidali L. F-Actin Mediated Focusing of Vesicles at
954 the Cell Tip Is Essential for Polarized Growth. Plant Physiol. 2018;176(1):352-63. Epub 20171002.
955 doi: 10.1104/pp.17.00753. PubMed PMID: 28972078; PubMed Central PMCID:
956 PMCPMC5761772.
957 65. Olson EN, Nordheim A. Linking actin dynamics and gene transcription to drive cellular
958 motile functions. Nat Rev Mol Cell Biol. 2010;11(5):353-65. Epub 2010/04/24. doi:
959 10.1038/nrm2890. PubMed PMID: 20414257; PubMed Central PMCID: PMCPMC3073350.
960 66. Knipe RS, Tager AM, Liao JK. The Rho kinases: critical mediators of multiple profibrotic
961 processes and rational targets for new therapies for pulmonary fibrosis. Pharmacol Rev.
962 2015;67(1):103-17. doi: 10.1124/pr.114.009381. PubMed PMID: 25395505; PubMed Central
963 PMCID: PMCPMC4279074.
964 67. Khatiwala CB, Kim PD, Peyton SR, Putnam AJ. ECM compliance regulates osteogenesis by
965 influencing MAPK signaling downstream of RhoA and ROCK. J Bone Miner Res. 2009;24(5):886-
966 98. doi: 10.1359/jbmr.081240. PubMed PMID: 19113908; PubMed Central PMCID:
967 PMCPMC2672206.
968 68. Zhong J, Yang Y, Liao L, Zhang C. Matrix stiffness-regulated cellular functions under
969 different dimensionalities. Biomater Sci. 2020;8(10):2734-55. Epub 20200423. doi:
970 10.1039/c9bm01809c. PubMed PMID: 32322859.
971 69. Luo YJ, Su YH. Opposing nodal and BMP signals regulate left-right asymmetry in the sea
972 urchin larva. PLoS Biol. 2012;10(10):e1001402. Epub 2012/10/12. doi:
973 10.1371/journal.pbio.1001402. PubMed PMID: 23055827; PubMed Central PMCID:
974 PMC3467216.
975 70. Siegel S, & Castellan, N. J., Jr. . Nonparametric statistics for the behavioral sciences 2ed:
976 Mcgraw-Hill Book Company; 1988.

71. Stalling D, Westerhoff M, Hege H-C. Amira: A highly interactive system for visual data analysis. The visualization handbook. 2005;38:749-67.